

Optics Letters

Multifiber angular compounding optical coherence tomography for speckle reduction

DONGYAO CUI,¹ EN BO,¹ YUEMEI LUO,¹ XINYU LIU,¹ XIANGHONG WANG,¹ SI CHEN,¹ XIAOJUN YU,¹ SHI CHEN,¹ PING SHUM,¹ AND LINBO LIU^{1,2,*}

¹School of Electrical and Electronic Engineering, Nanyang Technological University, Singapore 639798, Singapore

²School of Chemical and Biomedical Engineering, Nanyang Technological University, Singapore 637459, Singapore

*Corresponding author: liulinbo@ntu.edu.sg

Received 26 October 2016; revised 29 November 2016; accepted 29 November 2016; posted 5 December 2016 (Doc. ID 279096); published 23 December 2016

We report on an integrated fiber optic design to implement multifiber angular compounding optical coherence tomography, which enables angular compounding for speckle reduction. A multi-facet fiber array delivers three light beams to the sample with different incident angles. Back-reflective/back-scattered signals from these channels were simultaneously detected by a three-channel spectrometer. The axial and lateral resolution was measured to be ~ 3 and ~ 3.5 μm , respectively, in air with ~ 100 dB sensitivity. We conducted *ex vivo* experiments on a rat esophagus to demonstrate a contrast to noise improvement of 1.58. © 2016 Optical Society of America

OCIS codes: (170.4500) Optical coherence tomography; (170.3880) Medical and biological imaging.

<https://doi.org/10.1364/OL.42.000125>

With the ability to obtain real-time cross-sectional images at ~ 10 μm resolution, optical coherence tomography (OCT) has unique applications in the areas of clinical diagnostic imaging [1]. A new-generation high-resolution OCT, termed micro optical coherence tomography, has increased the resolution of conventional OCT by an order of magnitude in both axial and lateral dimensions and pushed the resolution to a ~ 1 μm scale, thus opening opportunities for high-resolution real-time pathology monitoring and disease diagnosis. However, despite the recent improvements in spatial resolution, some subtle, but important, tissue features remain unseen because OCT images are significantly confounded by speckle, a grainy pattern inherent to coherent detection systems [2]. Since these obscured details may include the critical features distinguishing healthy from diseased tissue, speckle reduction is of significant importance in disease diagnosis such as early cancer detection [3]. Speckle suppression techniques have been proposed and explored for better OCT image quality by compounding uncorrelated speckle patterns acquired at different polarizations, locations, times, or frequencies. Frequency compounding [4] and polarization compounding [5,6] have been successful in

speckle reduction, though the number of uncorrelated speckle patterns is achieved at the cost of axial resolution because of the splitting of the bandwidth in frequency compounding. Angular compounding has proven to be immune to such drawbacks and showed improved delineation of tissue microstructure. Angle variation by sequential selection [7,8] using a rotational/translational mirror can achieve large numbers of speckle patterns, but is unsuitable for *in vivo* application. Angular selection can be parallelized by multiplexing the detection, such as by array detector [9–11], joint aperture [12], Doppler-shift encoding [13], and path-length encoding [14]. The first three approaches suffer from some loss of lateral resolution due to the split of angular aperture, while path-length encoding has a decreased imaging range.

In this Letter, we present a new multifiber angular compounding OCT (MFOCT) imaging system using an angle-polished fiber array with a simultaneous multichannel spectrometer configuration that is free from degradations in resolution, imaging range, and sensitivity. A uniform-angle fiber array has been used to improve the imaging speed of OCT by applying multiple beams at the same time, but in different parts of the sample [15]. The system used an angular diversity fiber array design to implement the angular compounding method. The averaging of the angle-diversity data yields an improvement in the signal-to-noise ratio (SNR), contrast-to-noise ratio (CNR), and equivalent number of looks (ENL) without compromise in resolution and sensitivity. Improved image contrast was also observed.

The MFOCT system is depicted in Fig. 1. Near infrared (NIR) illumination is provided by a broadband supercontinuum light source (Supercontinuum Source SC-OEM, YSL, Wuhan Yangtze Soton Laser Co., Ltd.) over a spectrum from 400 to 2400 nm with total output power > 8 W. All the optical emission > 1000 nm was blocked by a short pass filter (DMSP1000, Thorlabs Inc.). We split the source output using a 70:30 (R:T) non-polarizing cubic beam splitter (BS1), followed by a 50:50 fiber coupler (Thorlabs Inc., TW850-R5A2) to further split into the second and third channels, and directed each beam to the input of three Michelson interferometer channels. The power distribution was 30%, 35%,

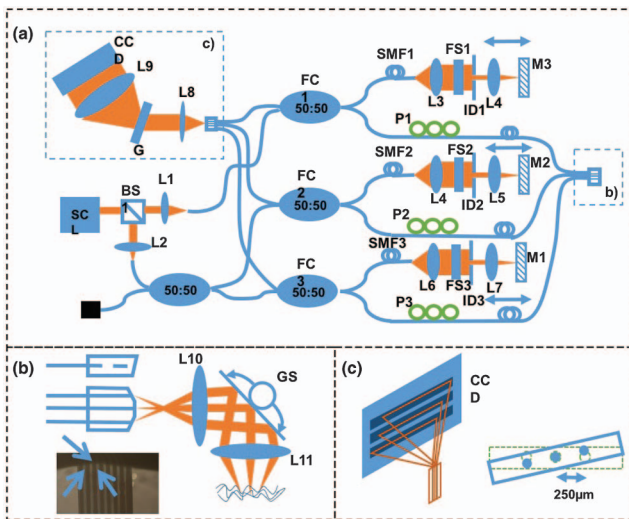


Fig. 1. Multifiber angular compounding optical coherence tomography system schematic. SCL, supercontinuum light source; L1-11, lenses; BS1, non-polarizing cube beam splitter; SMF1-3, single-mode fibers; M1-3, reference mirror; ID1-3, iris diaphragms; G, grating; GS, galvo scanners; P1-3, polarization controllers; FC1-3, 50:50 fiber couplers; FS1-3, fused silica dispersion compensators. (a) Overview system schematic. (b) Probe schematic to demonstrate the angle polish and angular diversity, and the image of the angle-polished fiber array tip. Three channels were implemented. The middle channel is flat polished, while the immediate adjacent channels were polished at 8 deg. The incident angle on sample was around 3.7 deg for the side channels at 320 μm spacing (figure not to scale). The channel spacing is 127 μm . The blue arrows show the active channels utilized in the proposed setup. (c) Spectrometer multichannel alignment illustration.

and 35% for channel 1, 2, and 3, respectively. In each channel, we used an additional 50:50 fiber coupler to split the reference arm and sample arm. The sample arm fibers of all three channels are terminated with a ν -groove array (VGA1) (VGA-8-127-0-X-14.4-4.0-2.03-S-780-5/125-3A-1-2-0.5-NF780HP, Wavelength Opto-Electronic) with 127 μm spacing. The reference fiber length was tailored to match that of the corresponding sample fiber and the residual material dispersion was further compensated by use of fused silicon blocks. Three paddle polarization controllers were used on the reference arm to adjust polarization and maximize interference fringe visibility.

As shown in Fig. 1(b), channel 1, 2 and 3 of VGA1 were angle-polished with respect to the horizontal axis (6390.1D, ULTRAPOL) at -8 , 0 , and 8 deg. In addition, all three channels are polished at 8 deg with respect to the vertical axis [Fig. 1(b)] to remove the Fresnel reflection at the fiber tip from the spectrometer input. In the benchtop probe, all three beams were collimated by an achromat (L8, AC050-010-B, Thorlabs Inc.), redirected by a galvo scanner and focused by objective lenses (AC050-016-B, Thorlabs Inc.) into focal spots with a theoretical full-width at half maximum diameter of 3.4 μm with slight displacements of 320 μm . Interference signals obtained from each channel were directed into another ν -groove array (VGA2) with channel spacing of 250 μm (VGA-8-250-0-X-14.4-4.0-2.03-S-780-5/125-3A-1-2-0.5-NF780HP, Wavelength Opto-Electronic) after passing the 2×2 fiber coupler and collimated

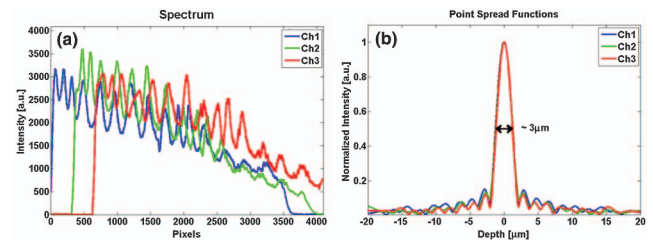


Fig. 2. (a) Multichannel spectrometer reference spectrum for the three channels obtained from the spectrometer configuration. Camera response introduces fringes in the spectrum. (b) Point spread functions for each individual channel. ~ 3 μm axial resolution in air was achieved.

by an achromat (L9, AC127-025-B-ML, Thorlabs Inc.) before entering the spectrometer [Fig. 1(c)]. The three-channel-spectrometer consisted of a 1765 lines/mm grating (PING-Sample-020, Ibsen photonics), a camera lens (Canon, EF 85 mm/1.2 II) and a three-line camera (EV71YM3-VCL4010-BAO, ELiXA 3V). The signal from each channel was detected separately by each individual CMOS linear array. VGA2 was rotated by 1.35 deg from horizontal to generate a 20 μm vertical offset to match the separation of the CMOS arrays [16]. We used ~ 3600 pixels to detect the signals with a bandwidth of 165 nm. Spectra were digitized at 12-bit resolution and transferred to the computer through camera link cables and an image acquisition board (KBN-PCE-CL4-F, Bitflow). Both camera and the galvo scanner were synchronized by a computer-generated trigger signal at an A-line rate of 5 kHz.

Standard OCT image processing was independently performed for each channel (background subtraction, interpolation and mapping from wavelength- to k - space and Fourier Transform [17]). To compensate for the fixed lateral displacement between foci, image registration was performed as a one-time calibration. The lateral shift was calibrated by scanning and matching a standard USAF-1951 resolution target and axial shift was optically compensated by adjusting the reference mirror position. Finally, images of different angles were compounded linearly and displayed on a logarithmic scale.

The theoretical axial resolution at 860 nm center wavelength of 165 nm bandwidth would be 2 μm for a perfectly Gaussian spectrum, though the actual axial resolution was slightly degraded because of the combined effects of the non-Gaussian source spectrum and the camera response. The experimental axial resolutions were measured to be 2.6, 2.9, and 3.2 μm , respectively, for the three channels (Fig. 2). The difference in axial resolution may come from spectrometer misalignment and spectrum calibration difference. As group 7 element 2 of USAF resolution target can be resolved for all channels, the lateral resolutions were measured to be approximately 3.48 μm .

To characterize the sensitivity of the system, we measured the SNR using a partially-reflecting mirror sample (-14 dB reflectivity) attenuated by a 14 dB neutral density filter. The path length difference between the sample and reference mirrors was maintained at 50 μm . The average incident power on the sample was approximately 5 mW from each channel at 180 μs exposure. The sensitivity for each camera line sensor was measured to be 98.5 dB, 100.1 dB, and 99.8 dB, respectively.

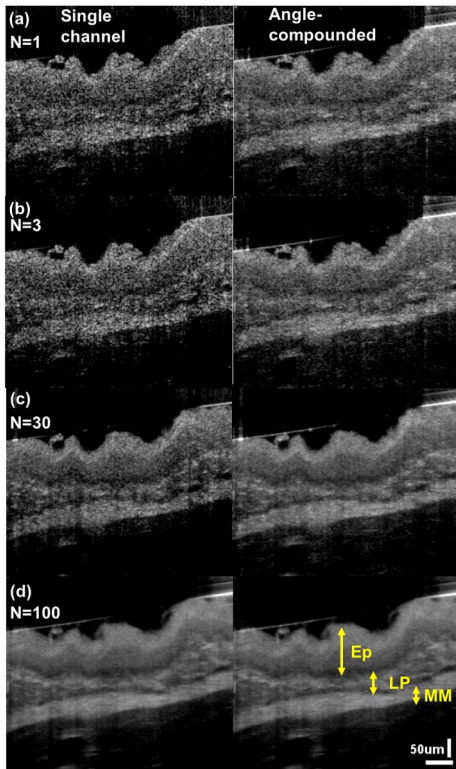


Fig. 3. Comparison of the speckle reduction effect using spatial compounding for a single channel and a multichannel. Better image contrast was observed for a multichannel system. (a)–(d) Left column, spatial compounding for single channel; right column, spatial compounding for a multichannel across 1, 3, 30, and 100 frames. Ep, epithelium; LP, lamina propria; MM, muscularis mucosae.

Ex vivo imaging experiments on rat esophagus were conducted at a frame rate of 10 Hz with 512 lines per frame per channel. Wild-type rat esophagus fresh tissue was dissected, kept in PBS solution and imaged within one hour of sacrifice. OCT images were acquired with the image size of 315×315 (axial \times transverse) pixels, corresponding to $600 \times 430 \mu\text{m}$.

Figure 3 compares images obtained without (left) and with (right) angular compounding technique. Spatial compounding was also implemented with varying frame numbers, $N = 1, 3, 30$ and 100 , and its speckle reduction effect were compared with that of angular compounding. Qualitatively, the amount of speckle reduction imparted by spatial compounding was minimal for $N < 10$; speckle remained largely correlated within this window. At $N = 30$, the contrast between layers improved, and a speckle reduction effect was more evident. Notably, a comparable speckle reduction result was achieved in a single frame by compounding images obtained by the three individual channels. By averaging different frames of angular compounded images, better image contrast and SNR was observed even with a single frame, since three uncorrelated speckle fields are available in a single shot.

One of the major drawbacks of spatial compounding speckle reduction is the degradation in lateral resolution. Averaging across more than 30 adjacent frames degrades resolution. With the multifiber angular compounding probe design, features were revealed that were originally obscured by speckle.

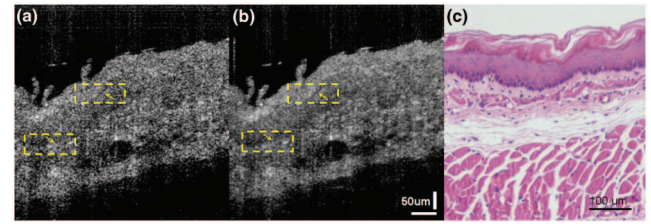


Fig. 4. Cross sections of a rat esophagus with three-frame averaging applied. (a) Single-channel result is highly obscured by speckle. (b) Multichannel image exhibits reduced speckle and better delineation (yellow arrows) that are concealed in (a). (c) Representative histology.

Figure 4 compares images obtained from a single channel (left) and multichannel (right), both averaged across three adjacent frames. The layered structure of rat esophagus was more distinguishable in speckle-reduced image [Fig. 4(b)]. The epithelium is better delineated from the overlying mucus and lamina propria beneath the basement membrane, which is not clearly distinguished with the conventional single-channel technique [Fig. 4(a)] due to speckle noise. This image quality improvement is confirmed by a representative histology image [Fig. 4(c)].

The image quality was also evaluated using well-established speckle-reduction performance metrics [18–22] for the esophagus images in Fig. 4, including SNR, CNR, and ENL, defined by the equations below. The CNR gives the contrast between a region of interest and a region of background noise, while the ENL measures the smoothness of the speckle-corrupted homogenous region:

$$\text{SNR} = 10 \log_{10} \left(\max \frac{S_{\text{lin}}^2}{\sigma_{\text{lin}}^2} \right),$$

$$\text{CNR} = \frac{1}{R} \sum_{r=1}^R (\mu_r - \mu_b) / \sqrt{\sigma_r^2 + \sigma_b^2},$$

$$\text{ENL} = \frac{1}{H} \sum_{h=1}^H \mu_h^2 / \sigma_h^2.$$

In the above equations, S_{lin} and σ_{lin}^2 are the magnitude of image and variance of the background noise region from linear OCT images, μ_b and σ_b^2 are the mean and variance of the same background from logarithmic OCT images, μ_h and σ_h^2 are the mean and variance of all the homogeneous regions of interest (H), and μ_r and σ_r^2 are the mean and variance of all the regions of interest (R), including the homogeneous regions (H) from logarithmic OCT images. The distance between the adjacent A -lines was $1.37 \mu\text{m}$, which is less than half of the beam diameter; thus, the window size was chosen to be 5×5 pixels for $H = 5$ and $R = 9$. The homogenous regions were chosen

Table 1. SNR, CNR, and ENL for Single-Channel and Angular-Compounded Images

	Single	Compounded	Improvement
SNR	43.81 dB	45.32 dB	1.51 dB
CNR	3.95	6.26	1.58
ENL	183.59	463.99	2.53

within a single tissue layer, whereas the non-homogenous regions were chosen at tissue layer boundaries across two different tissue layers.

The SNR, CNR, and ENL for single- and angle-compounded OCT images were investigated. The center channel was selected for single-channel evaluation because its sensitivity and lateral resolution were the highest among the three channels. The SNR, CNR, and ENL were evaluated and averaged over 50 frames.

The SNR improved by 1.51 dB for an angle-compounded image. We attribute the difference between the experimental values to the theoretical value of 2.39 dB to the coherence of the speckle noise in the three channels. The CNR improved by 1.58 for an angular-compounded image. The ENL also has significant improvement by a factor of 2.53 for an angular-compounded image (Table 1).

Though we demonstrated the speckle reduction capability of the current optical design, improved performance can be achieved with further design optimization. First, the 127 μm fiber core spacing caused the three beams to propagate with such a diverging angle after passing the probe collimation lens that an objective lens with a large aperture was required to enclose all three input beams. Consequently, this optical pre-arrangement rules out the possibility of achieving high lateral resolution using a low-cost objective lens. Second, the speckle reduction effect scales with the number of channels, which was only three in the current setup. Both problems could be addressed by replacing the fiber array with a more compact multibeam endoscopic probe configuration similar to [23] or a multicore fiber. These approaches would increase fiber density, increasing the number of channels and reducing the space between different channels, as well as enabling a more compact and flexible imaging probe. Lastly, we used a relatively low imaging speed in this proof-of-concept study, which is not enough for most of *in vivo* applications. This data throughput issue can be solved by improving imaging the acquisition and display program. An increased number of channels, reduced space between different channels, and improved data acquisition speed in this design would improve the technical feasibility of the implementation of the technique and contribute significantly to *in vivo* clinical translational studies.

In conclusion, we successfully demonstrated a MFOCT system for speckle reduction in spectral domain OCT. A fiber optic multichannel system is better than a free-space multichannel system because of its ease of construction and maintenance, which also increases clinical usability [12]. The key element—angle polished fiber array—can be implemented in an endoscopic or intravascular probe by reducing the channel spacing or use of a multicore fiber. The speckle-reduced images exhibited better image contrast, SNR, CNR, and ENL, compared to the original images without loss of resolution. These advances in image quality will be particularly useful for visualization of cellular and subcellular structures which suffer most from speckle noise [24,25].

While substantial speckle reduction was seen with our present system, improving system performance by increasing fiber density using a multicore fiber will be a subject of future development.

Funding. National Research Foundation Singapore (NRF) (NRF-CRP13-2014-05); National Medical Research Council (NMRC) Singapore (NMRC/CBRG/0036/2013); Ministry of Education - Singapore (MOE) (MOE2013-T2-2-107); NTU-AIT-MUV Program in Advanced Biomedical Imaging (NAM/15005); Nanyang President Graduate Scholarship.

Acknowledgment. The authors gratefully acknowledge the advice and mental support from Dr. Kengyeh Chu in the manuscript preparation.

REFERENCES

1. D. Huang, E. A. Swanson, C. P. Lin, J. S. Schuman, W. G. Stinson, W. Chang, M. R. Hee, T. Flotte, K. Gregory, C. A. Puliafito, and G. F. James, *Science* **254**, 1178 (1991).
2. J. M. Schmitt, S. H. Xiang, and K. M. Yung, *J. Biomed. Opt.* **4**, 95 (1999).
3. Y. T. Pan, Z. L. Wu, Z. J. Yuan, Z. G. Wang, and C. W. Du, *J. Biomed. Opt.* **12**, 050504 (2007).
4. M. Pircher, E. Götzinger, R. Leitgeb, A. F. Fercher, and C. K. Hitzenberger, *J. Biomed. Opt.* **8**, 565 (2003).
5. T. Storen, A. Royset, N.-H. Giskeodegard, H. M. Pedersen, and T. Lindmo, *Proc. SPIE* **5316**, 196 (2004).
6. J. F. de Boer, S. M. Srinivas, B. H. Park, T. H. Pham, Z. Chen, T. E. Milner, and J. S. Nelson, *IEEE J. Sel. Top. Quantum Electron.* **5**, 1200 (1999).
7. M. Hughes, M. Spring, and A. Podoleanu, *Appl. Opt.* **49**, 99 (2010).
8. A. E. Desjardins, B. J. Vakoc, W. Y. Oh, S. M. Motaghianezam, G. J. Tearney, and B. E. Bouma, *Opt. Express* **15**, 6200 (2007).
9. Y. Watanabe, H. Hasegawa, and S. Maeno, *J. Biomed. Opt.* **16**, 060504 (2011).
10. A. E. Desjardins, B. J. Vakoc, G. J. Tearney, and B. E. Bouma, *Opt. Express* **14**, 4736 (2006).
11. J. M. Schmitt, *Phys. Med. Biol.* **42**, 1427 (1997).
12. T. Klein, R. André, W. Wieser, T. Pfeiffer, and R. Huber, *Biomed. Opt. Express* **4**, 619 (2013).
13. H. Wang and A. M. Rollins, *J. Biomed. Opt.* **14**, 030512 (2009).
14. N. Iftimia, B. E. Bouma, and G. J. Tearney, *J. Biomed. Opt.* **8**, 260 (2003).
15. C. Zhou, A. Alex, J. Rasakanthan, and Y. Ma, *Opt. Express* **21**, 19219 (2013).
16. E. Bo, X. Liu, S. Chen, X. Yu, X. Wang, and L. Liu, *Opt. Express* **23**, 28050 (2015).
17. M. Wojtkowski, V. J. Srinivasan, T. H. Ko, J. G. Fujimoto, A. Kowalczyk, and J. S. Duker, *Opt. Express* **12**, 2404 (2004).
18. K. M. Yung, S. L. Lee, and J. M. Schmitt, *J. Biomed. Opt.* **4**, 125 (1999).
19. J. Rogowska and M. E. Brezinski, *IEEE Trans. Med. Imaging* **19**, 1261 (2000).
20. D. C. Adler, T. H. Ko, and J. G. Fujimoto, *Opt. Lett.* **29**, 2878 (2004).
21. D. L. Marks, T. S. Ralston, and S. A. Boppart, *J. Opt. Soc. Am. A* **22**, 2366 (2005).
22. A. Ozcan, A. Bilenca, A. E. Desjardins, B. E. Bouma, and G. J. Tearney, *J. Opt. Soc. Am. A* **24**, 1901 (2007).
23. A. S. Beau, K. C. L. Kenneth, M. Adrian, R. M. Nigel, K. K. L. Michael, X. D. Y. Victor, and I. A. Vitkin, *Phys. Med. Biol.* **55**, 615 (2010).
24. M. Kashiwagi, L. Liu, K. K. Chu, C.-H. Sun, A. Tanaka, J. A. Gardecki, and G. J. Tearney, *PLoS ONE* **9**, e102669 (2014).
25. D. Cui, X. Liu, J. Zhang, X. Yu, S. Ding, Y. Luo, J. Gu, P. Shum, and L. Liu, *Opt. Lett.* **39**, 6727 (2014).